ACS Sustainable Chemistry & Engineering

pubs.acs.org/journal/ascecg

Research Article

In Situ Doping-Enabled Metal and Nonmetal Codoping in Graphene Quantum Dots: Synthesis and Application for Contaminant Sensing

Aruna N. Nair, Venkata S.N. Chava, Saptasree Bose, Ting Zheng, Srikanth Pilla, and Sreeprasad T. Sreenivasan*

Cite This: *ACS Sustainable Chem. Eng.* 2020, 8, 16565−16576

Read Online

ACCESS | Metrics & More | Article Recommendations | Supporting Information

ABSTRACT: Fluorescent graphene quantum dots (GQDs) prepared from low-cost and sustainable precursors are highly desirable for various applications, including luminescence-based sensing, optoelectronics, and bioimaging. Among different natural precursors, the unique structural and compositional variety and the abundance of aromatic carbon in lignin make it a unique and renewable precursor for the green synthesis of advanced carbon-based materials including GQDs. However, the inferior photoluminescence quantum yield of GQDs prepared from natural precursors, including lignin, limits their practical utility. Here, for the first time, we demonstrate that the presence of heteroatoms in the innate structure of lignosulfonate can be leveraged to derive in situ heteroatom-doped GQDs with excellent photophysical properties. The as-synthesized lignosulfonate-derived GQDs showed compelling blue fluorescence with a high quantum yield of 23%, which is attributed to in situ S and N doping as confirmed by using X-ray photoelectron spectroscopy and Fourier transform infrared spectroscopy analyses. Assisted by the in situ doping, we further engineered the lignosulfonate-derived GQDs by incorporating a metal atom dopant to derive an enhanced quantum yield of 31%, the highest for any lignin-derived GQDs. Moreover, fundamental photoluminescence studies reveal the presence of multiple emissive centers, with edge states acting as dominant emission centers. Finally, we also demonstrate the applicability of the luminescent, metal- and nonmetal-codoped lignin-derived GQDs as a highly selective sensor for the sub-nanomolar level detection of mercuric ions in water.

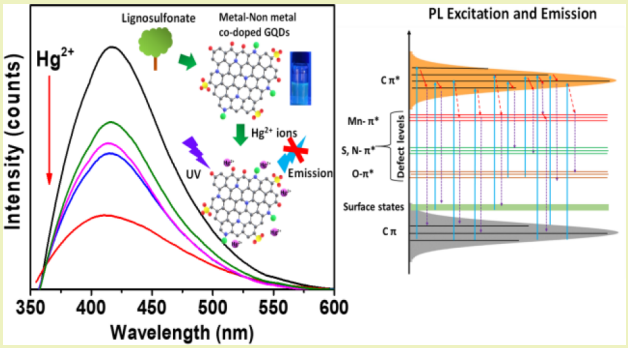

KEYWORDS: *lignosulfonate, graphene quantum dots, hydrothermal synthesis, in situ S,N doping, metal doping, photoluminescence, mercury detection*

Downloaded via UNIV OF TEXAS AT EL PASO on April 26, 2021 at 20:51:24 (UTC).
See https://pubs.acs.org/sharingguidelines for options on how to legitimately share published articles.

INTRODUCTION

Graphene quantum dots (GQDs), because of their carbon-based structure, demonstrate excellent material properties such as high water dispersibility, ease of functionalization, biocompatibility, and chemical inertness. Triggered by quantum confinement effects, GQDs possess superior optical and electronic properties that can be leveraged for bioimaging, biosensors, drug delivery, luminescence-based contaminant sensing, photocatalysis, solar cells, and light-emitting diodes.[1−6] GQDs with a tailored structure can be synthesized from their corresponding precursors through chemical disproportionation, carbonization, or pyrolysis.[7−10] However, common synthetic precursors employed for GQD synthesis are nonrenewable, expensive, and not eco-friendly. Hence, synthesis of GQDs from sustainable and inexpensive precursors, including biomass/food wastes and biomass byproducts, has attracted significant research interest recently.[11−17] Because common biomass-derived materials (e.g., cellulose) do not contain aromatic rings, their conversion to GQDs requires additional energy to form phenyl rings. Hence, it is advantageous to choose precursors that contain aromatic rings in their native structure for GQD synthesis.

Lignin, the second most abundant biopolymer, with a highly cross-linked structure composed of a phenyl-based skeleton, is potentially an ideal precursor for the facile synthesis of advanced materials with aromatic subunits such as GQDs. Lignin can be categorized as alkali lignin, Kraft lignin, hydrolyzed lignin, organosolv lignin, and lignosulfonates based on the extraction process used. Different lignin forms differ not only in their intricate structure but also in terms of the elemental composition. Despite its promise, lignin is critically underutilized, with ∼98% of lignin produced annually being used as a heat source.[18] Of the remaining 2%, the

Received: August 7, 2020
Revised: October 2, 2020
Published: October 28, 2020

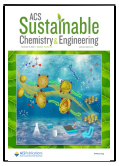

ACS Publications

© 2020 American Chemical Society

majority is applied in low return-on-investment applications, such as concrete admixtures, dispersants, and pellet binders. Because of its environmental and economic advantages, researchers started to exploit the aromatic content in lignin to produce various chemicals and carbonaceous nanomaterials, including carbon fibers, graphene, and carbon nanotubes.[19−23] Recently, GQDs have also been synthesized from alkali lignin through a simple reorganization and refusion of aromatics.[15] However, similar to other renewably resourced GQDs, lignin-derived GQDs showed inferior properties compared to their counterparts synthesized from synthetic precursors. For example, the photoluminescence quantum yield (PLQY) of alkali lignin-derived GQDs was 21%, lower than the PLQYs of GQDs synthesized from nonrenewable precursors, thus limiting their potential use.[15]

Heteroatom doping in the GQD lattice (i.e., the introduction of noncarbon foreign atoms) is routinely performed to enhance the quantum-enabled properties of GQDs. Conventionally, doping is achieved through the addition of the coreactants consisting of dopant atoms in the synthesis process. In addition to influencing quantum confinement, surface functional groups, and edge effects, heteroatom doping is also known to introduce more active vacancies and significantly alter GQD intrinsic characteristics. For example, PL, one of the most exciting properties of GQDs, is known to get amplified by doping GQDs with nonmetal or metal heteroatoms.[24,25] Especially, the PLQY was significantly increased upon doping because of the creation of new defects/edge states in GQDs.[26,27] Though doping of GQDs is practiced extensively, efforts to augment the properties of lignin-derived GQDs through doping are in its infancy. Previous studies on alkali lignin-derived GQDs by Ding et al.[15] through N-doping and Wang et al.[28] through S and N codoping lead to a constant PLQY of 21%. The inadequacy of simple doping strategies to increase the PLQY in lignin-derived GQDs indicates that enhancing the PLQY in these systems is not trivial. Typically, doping GQDs with different elements (codoping) can significantly enhance their properties through synergistic effects.[29,30] Though codoping using different nonmetals is frequently performed, studies on metal−nonmetal codoping in the GQD matrix are minimal, probably because of the increased complexity of the reaction.[24,31−33] Nonetheless, codoping of metals and nonmetals in GQDs leads to superior properties because of the creation of more defect sites, the increased availability of vacant energy levels, and the synergistic electron-donating/withdrawing ability of dopants.

To the best of our knowledge, the metal−nonmetal codoping or simple metal atom doping is not explored previously in lignin-derived GQDs. Because nonmetal doping/codoping did not result in an increase in the PLQY of lignin-derived GQDs, it is imperative to expand the doping to metal- and nonmetal-codoping strategy. Here, for the first time, we demonstrate that by coreacting lignosulfonate that contain heteroatoms (S and N) in its structure[34] and a metal precursor, metal- and nonmetal-codoped GQDs with significantly enhanced optical properties can be synthesized. The S and N atoms present in lignosulfonate lead to in situ doping with S and N, while the external metal precursor helps to integrate the metal atoms. Because of the reported ability of manganese (Mn) to enhance the photophysics of GQDs,[24] Mn was selected as a model metal dopant. By synthesizing lignosulfonate-derived, in situ S and N-codoped GQDs (LGQDs) and LGQDs containing Mn (Mn-LGQDs), we also investigated the emissive centers in the LGQDs with and without Mn doping and, from a fundamental band structure point of view, explained the observed changes in the luminescence properties. The luminescence of GQDs is extremely sensitive to the ionic environment of the solution, which can be used for detecting the external ions in the ensemble. Hence, the GQDs can be employed for the sensitive detection of contaminants in water samples.[30,35−39] Capitalizing on the excellent PL of the Mn-LGQDs, we further illustrate their potential for the selective sub-nanomolar detection of mercuric ions, a water contaminant with acute toxicity,[40] in drinking water.

MATERIALS AND METHODS

Materials and Chemicals. All chemicals and reagents used in this work were commercially available, of analytical grade, and used as received without any further purification unless otherwise specified. Lignosulfonic acid sodium salt (MW ∼52,000) was purchased from Beantown chemicals, and precursor salts $MnCl_2$, $CuCl_2$, $ZnCl_2$, $AgNO_3$, $CoCl_2$, $NiCl_2$, $FeCl_2$, $Cd(NO_3)_2$, $MgCl_2$, $CaCl_2$, $Pb(NO_3)_2$, and $Hg(NO_3)_2$ were purchased from Alfa Aesar. Nitric acid (70%) was used for LGQD synthesis, and quinine sulfate (the standard sample used for PLQY measurements) and $HgCl_2$ were purchased from Millipore Sigma. Stock solutions of Hg^{2+}, Ag^{+}, Ca^{2+}, Cd^{2+}, Co^{2+}, Cu^{2+}, Fe^{3+}, Mg^{2+}, Mn^{2+}, Zn^{2+}, Ni^{2+}, and Pb^{2+} ions were prepared by dissolving their corresponding metal salts in deionized (DI) water. Ethylenediaminetetraacetic acid (EDTA) was purchased from Millipore Sigma.

Synthesis of Doped GQDs from Lignin. The synthesis of both LGQDs and Mn-LGQDs was performed by following a modified hydrothermal method,[15] as described below. It is to be noted that there was a minor difference in the case of Mn-LGQD synthesis, in which an additional Mn precursor salt was added to the reaction mixture. For the LGQD synthesis, first, 3 g of lignosulfonic acid sodium salt was dissolved in 15 mL of DI water. Then, 5 mL of nitric acid was gradually added to that solution with continuous stirring. The resulting dispersion was ultrasonicated for 12 h (at 40 kHz frequency and 110 W) and diluted with DI water. The dispersion was vacuum-filtered using a 0.22 μm microporous membrane, and the residue was redispersed in 40 mL of DI water to create a carbonized precursor. Subsequently, the precursor solution was transferred to a teflon-lined autoclave for the hydrothermal reaction at 200 °C. To introduce Mn into the LGQDs, $MnCl_2$ was added (0.6−4% by weight) as a coreactant into the hydrothermal reaction mixture. The hydrothermal reaction parameters including temperature, duration, dopant concentration, and so forth were varied to optimize the reaction conditions. The hydrothermal reaction product was filtered through a 0.22 μm microporous membrane to remove insoluble carbon. The brown filtrate was then centrifuged at 20k rpm for 30 min, and the supernatant containing LGQDs was collected. Finally, the supernatant with LGQDs was lyophilized and stored as a powder.

PL-Based Detection of Hg^{2+} Ions in Water Samples. For mercuric (Hg^{2+}) ion-sensing studies, the LGQD sample solutions (0.1 mg/mL) were mixed with calculated amounts of Hg^{2+} ions (in the range of 2 nM to 1 μM), and the resultant changes in fluorescence spectra were investigated. Similarly, for Mn-LGQDs (2% doping), a pH of 5.5 and a solution concentration of 0.1 mg/mL were used, where the maximum PL emission intensity was observed. The PL spectrum was recorded by fixing the excitation wavelength (λ_{ex}) at 340 nm. In a typical experiment, the PL spectra of the LGQD/Mn-LGQDs were first measured under an ideal excitation condition, followed by the PL spectra measurement after the addition of Hg^{2+} solution. Throughout this study, the volume of Hg^{2+} (different concentrations) introduced into the LGQD/Mn-LGQD mixture was kept constant to mitigate dilution-based effects. The dilution effect on luminescence was evaluated by the addition of an equal volume of DI water to the LGQD/Mn-LGQDs. The selectivity of Mn-LGQDs toward Hg^{2+} detection was investigated by studying the luminescence spectra of the Mn-LGQD solution containing different metal ions

https://dx.doi.org/10.1021/acssuschemeng.0c05789
ACS Sustainable Chem. Eng. 2020, 8, 16565−16576

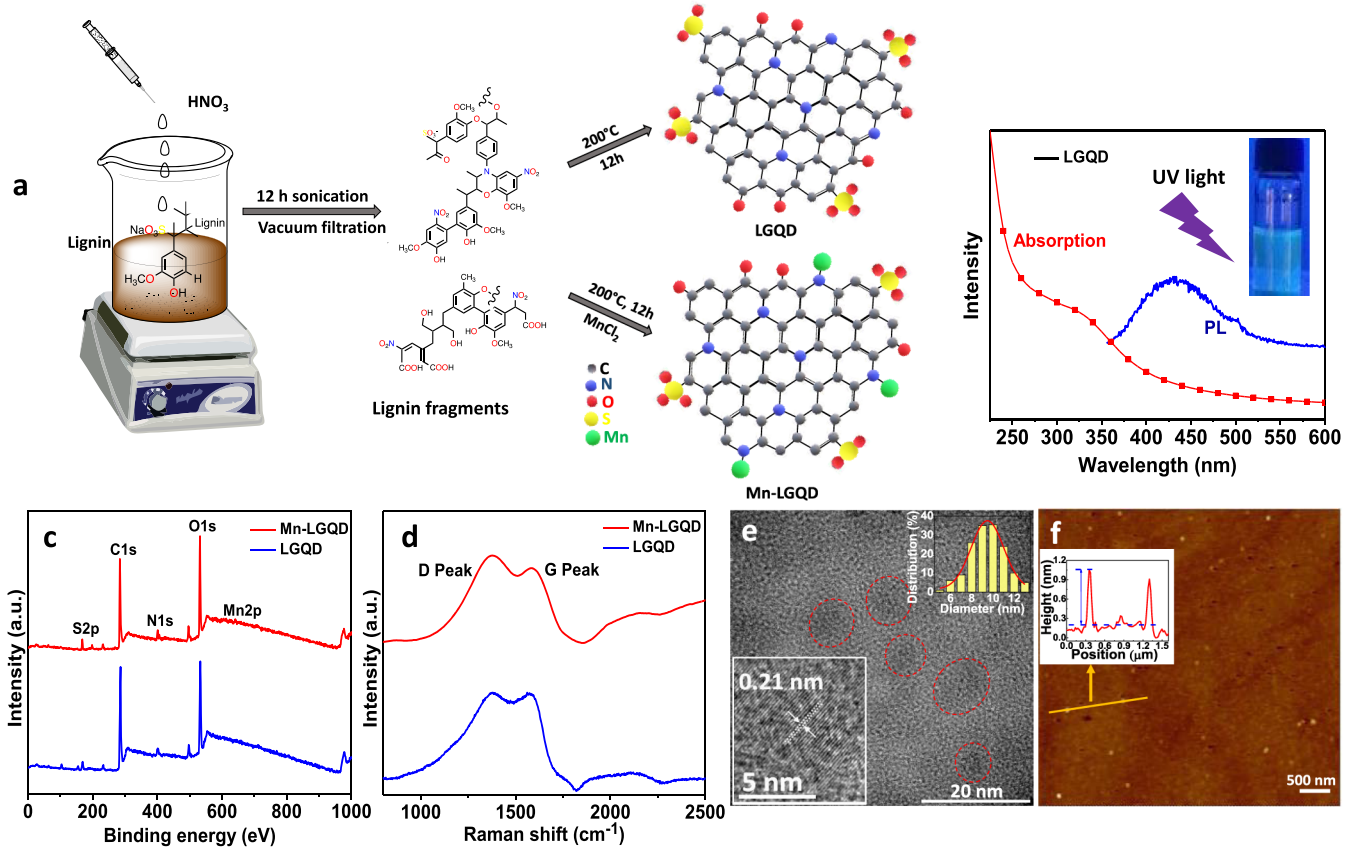

Figure 1. (a) Schematic of the hydrothermal synthesis of LGQDs and Mn-LGQDs. (b) UV−vis absorption and PL emission spectra of LGQDs. The inset shows a photograph of LGQDs emitting blue light when excited with a UV lamp. (c) XPS survey spectra of LGQDs and Mn-LGQDs and (d) Raman spectra of LGQDs and Mn-LGQDs. (e) TEM image of Mn-LGQDs; scale bar is 20 nm. (Inset at the top right shows the histogram for the Mn-LGQD size distribution, and the bottom inset shows the HRTEM image; scale bar is 5 nm). (f) AFM topography image of Mn-LGQDs; scale bar is 500 nm. (Inset shows the height scan of the Mn-LGQDs indicated by the arrow).

prepared, as explained above. The PL spectrum of the Mn-LGQDs was first measured under an optimal excitation wavelength of 340 nm. Subsequently, a specific concentration of Hg^{2+} solution (250 and 1000 nM) was added to the LGQD solution and the PL spectrum was analyzed after the addition of the ions, to observe PL quenching. In order to regain PL, we added stoichiometric amounts of EDTA solution into the mixture and it was sonicated for 10 min. Finally, the PL spectrum was remeasured to observe the increased intensity. After PL regain experiments, we further tested the reusability of the GQD-based sensors using 250 nM Hg^{2+} concentration. The sensing of low and high concentrations of Hg^{2+} was also performed in tap water.

RESULTS AND DISCUSSION

Our synthetic process, which converts lignosulfonate into LGQDs with a designed architecture, follows a two-step hydrothermal process that includes oxidative scission and aromatic reintegration (Figure 1a).[41] Here, the oxidative scission was performed with nitric acid, and the resultant lignosulfonate segments were further aromatically re-fused into crystalline LGQDs via the hydrothermal treatment. A coreactant ($MnCl_2$) was added to the cleaved and carbonized lignosulfonate fragments to incorporate Mn atoms in the LGQD lattice for Mn-LGQD's synthesis. When irradiated with a UV lamp, the LGQD sample solutions emitted an intense blue light because of the quantum confinement-induced band gap effect, indicating the successful formation of GQDs. Figure 1b shows a representative absorbance and PL spectra of LGQDs and a photograph of the blue light-emitting LGQD solution (inset of Figure 1b). Previous studies suggested that the hydrothermal process parameters can control the size, surface chemistry, and resultant properties of GQDs.[6] Hence, we systematically varied the process parameters that include hydrothermal reaction temperature and time to tune the size and surface chemistry of LGQDs and to optimize their PLQY, which is a critical aspect of the study. First, we prepared different LGQD samples at reaction temperatures of 160, 180, 200, and 210 °C by keeping the reaction duration (12 h) constant. The PL measurements showed a maximum intensity for the sample synthesized at 200 °C (Figure S1a). In a similar study carried out at a constant reaction temperature of 200 °C for different reaction durations, the maximum PL was observed (Figure S1b) for a reaction time of 12 h. Thus, we confirmed that a reaction temperature of 200 °C and duration of 12 h are optimal for procuring LGQDs with superior PL. The PL properties did not show a significant change when the initial concentration of lignosulfonate was varied. For Mn-LGQDs, we also investigated the effect of heteroatom concentration on the PL intensity. Figure S2 shows the PL spectra of Mn-LGQDs, with Mn doping percentage varied from 0.6 to 4%. The dopant percentages referred here are the initial weight percentage of dopant precursors introduced into the hydrothermal reaction. As shown in Figure S2, PL spectra demonstrated a strong dopant concentration dependence. From this figure, it is evident that the 2% doping of Mn yielded the highest QY when compared to the other dopant

https://dx.doi.org/10.1021/acssuschemeng.0c05789
ACS Sustainable Chem. Eng. 2020, 8, 16565−16576

Table 1. Atomic Percentages of Different Elements in Lignosulfonate, LGQDs, and Mn-LGQDs

	element						
			N 1s				
sample	C 1s	O 1s	graphitic	pyridinic	S 2p	Mn 2p	QY %
lignosulfonate	65.6	30.09	1.03	0.32	2.96	0	
LGQD	67.87	24.93	4.33	0.56	2.31	0	23
Mn-LGQD	63.67	26.97	5.15	1.36	2.61	0.24	31.6

concentrations. The PLQY was found to be lower for concentrations below or above 2%. The strong dopant concentration-dependent PL demonstrated by Mn-LGQDs suggests that even a minimal change in the dopant concentration can substantially alter their optical activity. A decrease in PL intensity was observed, as we increased the doping percentage above the optimal doping. A similar PL response with doping was reported in the study by Kadian et al.[42] One of the mechanisms for an enhanced PLQY for functionalized GQDs is the surface passivation of defects by functional groups.[43−45] However, upon increasing the number of dopants (Mn in the present case), the integration of dopants into the GQD lattice can not only create more defects, but also disrupt the passivation effects by metal coordination with the functional groups. Hence, beyond optimal concentration of the dopant, the newly created defects (which could function as the quenching centers) in combination with the reduced surface passivation lead to a decrease in the quantum yield.[42,46−48]

The GQD samples were analyzed using X-ray photoelectron spectroscopy (XPS) to ascertain the success of doping. The XPS survey scan of LGQDs demonstrated features at 167.72, 284.5, 398.58, and 532.14 eV, corresponding to the binding energies of S 2p, C 1s, N 1s, and O 1s, confirming the presence of C, O, N, and S in the LGQD (Figure 1c), respectively. Because the XPS analysis confirmed the existence of S and N in the lignosulfonate precursor (Figure S3), it is prudent to hypothesize that the use of lignosulfonate with S and N in its native structure leads to the formation of in situ S and N-doped LGQDs. It is worth noting that besides the S and N atoms present in the lignosulfonate precursor, the N atoms from the nitric acid treatment during synthesis also likely contribute toward N doping in LGQDs.[15] The XPS survey scan for Mn-LGQDs (Figure 1c), in addition to S 2p, C 1s, N 1s, and O 1s, illustrated a feature at 642.29 eV corresponding to Mn 2p, confirming the successful metal (Mn)−nonmetals (S and N) codoping in the Mn-LGQDs. Table 1 shows the atomic percentages of elements present in the lignosulfonate, LGQDs, and Mn-LGQDs calculated from the XPS data. The elemental quantification indicated a relatively lower carbon content in the case of Mn-LGQDs compared to LGQDs (Table 1). The observed lower carbon content could be attributed to the replacement of C atoms in the lattice by dopant atoms via substitutional doping (mostly O and N). Hence, the XPS characterization results confirmed that aided by in situ doping afforded by the lignosulfonate precursor, Mn, S, and N atoms get incorporated into the Mn-LGQDs, resulting in a metal−nonmetal-codoped GQD system.

After confirming the successful formation of the doped GQDs, the samples were analyzed using different microscopic and spectroscopic techniques to derive in-depth understanding regarding their morphology, structure, surface chemistry, and photophysics. The XRD spectra of LGQDs showed a broad peak at 2θ = 26.5° (corresponding to the (002) plane), indicating the presence of the graphitic lattice (Figure S4). The graphenic structure and the defect density of LGQDs and Mn-LGQDs were evaluated using Raman spectroscopy. The Raman spectra of LGQDs and Mn-LGQDs (Figure 1d) showed a prominent G-band at ∼1570 cm^{-1} corresponding to the first-order scattering or the E_{2g} vibrational mode of the sp^2 carbons, emphasizing the presence of graphenic regions.[49] Another prominent feature appeared in the Raman spectra at ∼1375 cm^{-1} called the D-band points to the disorder in both LGQDs and Mn-LGQDs. Hence, Raman studies also confirmed the conversion of the polymeric lignosulfonate into LGQDs, complementing the XPS and XRD data. In general, the intensity ratio (I_D/I_G) of the D-band and G-band is considered a quantitative measure of the defect density in graphenic matrices. Our analysis indicated that the I_D/I_G is higher for Mn-LGQDs (1.17) when compared to LGQDs (1.01). The higher I_D/I_G ratio is plausibly due to the introduction of a relatively higher number of defects in Mn-LGQDs compared to LGQDs. Figure 1e,f shows the morphological and topographical images of the Mn-LGQDs obtained using TEM and AFM. The TEM image and its corresponding size-distribution histograms (insets of Figures 1e and S5) clearly show that Mn-LGQDs and LGQDs have an average size of ∼10 nm. The lattice-resolved HRTEM image (inset of Figure 1e) depicts a characteristic (010) plane of the graphitic lattice with an interplanar distance of 0.21 nm, indicating the crystalline, graphenic nature of LGQDs and Mn-LGQDs. The AFM topography and a representative height scan profile for Mn-LGQDs (inset) are shown in Figure 1f. The ∼1 nm height calculated here indicates that Mn-LGQDs consist of a maximum of three graphene layers. However, it was previously reported that even single-layer solution-dispersed GQDs can show height profiles up to 1 nm in AFM.[50] AFM images corresponding to LGQDs are shown in Figure S6b. After evaluating the structural and morphological properties of LGQDs, we probed the surface chemistry of LGQDs and Mn-LGQDs using Fourier transform infrared (FTIR) and high-resolution XPS. Figure S7 shows the FTIR spectra of lignosulfonate, LGQD, and Mn-LGQD samples. The presence of vibrational bands at 1600 cm^{-1} (aromatic C=C stretching vibration), 1091, 830, and 798 cm^{-1} (the in-plane and out-of-plane deformations of aromatic C−H) confirmed the preservation of aromatic moieties during the conversion of lignosulfonate to LGQDs. Furthermore, the C−O−C linkages (ether) found in lignosulfonate did not exist in the IR spectrum of LGQDs (and Mn-LGQDs), indicating the cleavage of ether during the LGQD formation. The IR spectra of LGQDs also showed a broad vibrational band at 3350 cm^{-1} (OH vibration), 1637 and 1191 cm^{-1} (C=O and C−O), representing the edge functional groups, including ketones, carboxylic acids, and alcohols.

Besides, LGQDs and Mn-LGQDs also exhibited a vibrational feature at 1404 cm^{-1}, which could result from C−N or S=O vibration, signifying the lattice incorporation of nitrogen and/or sulfur.[51] The peak observed around 1350 cm^{-1} in

https://dx.doi.org/10.1021/acssuschemeng.0c05789
ACS Sustainable Chem. Eng. 2020, 8, 16565−16576

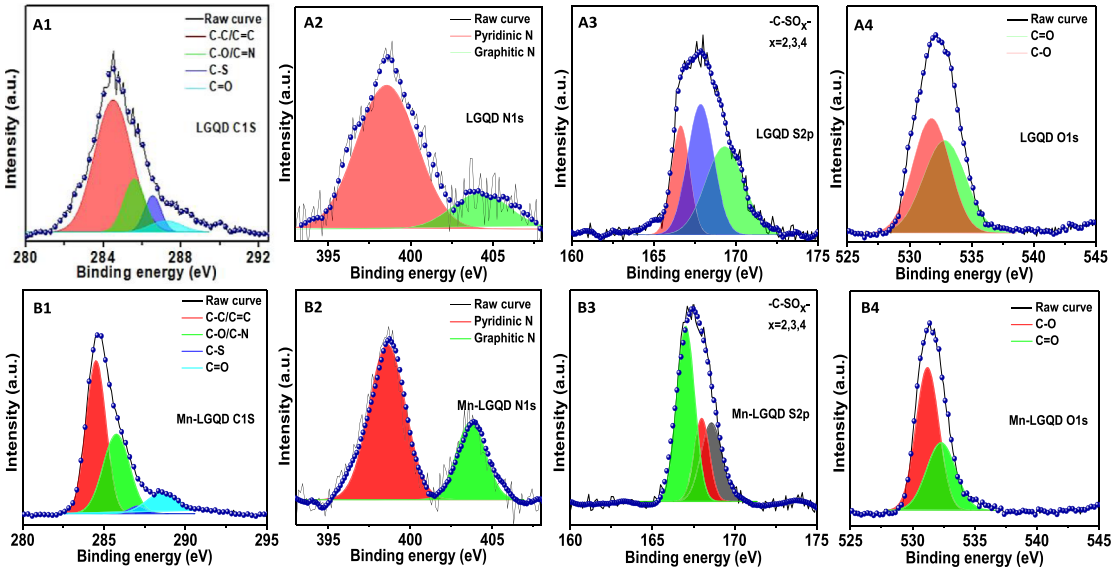

Figure 2. High-resolution XPS spectra corresponding to C 1s, N 1s, S 2p, and O 1s of LGQDs (A1−A4) and Mn-LGQDs (B1−B4).

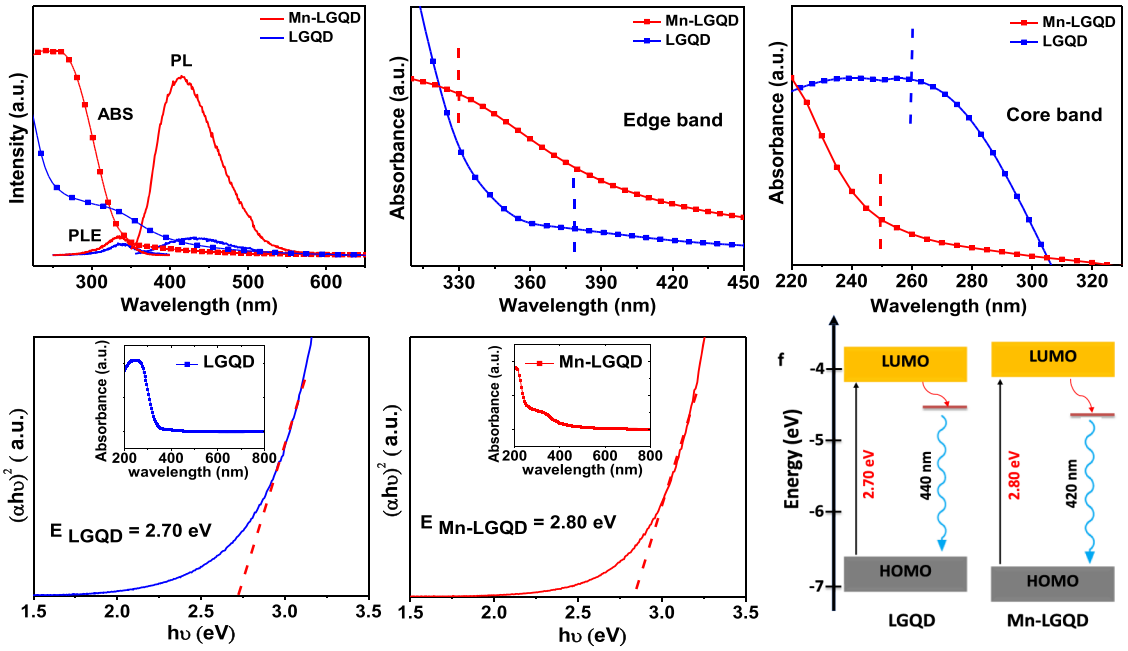

Figure 3. (a) UV−vis absorbance spectra, PL excitation, and PL emission (PL) of LGQDs and Mn-LGQDs. (b,c) Core band and edge band observed in the absorbance spectra of LGQDs and Mn-LGQDs. (d,e) Band gap measurement using Tauc plots for LGQDs and Mn-LGQDs (inset shows the corresponding UV−vis absorbance spectrum). (f) Schematic showing the band structure and its corresponding PL. As shown here, the optical band gap of Mn-LGQDs is higher compared to LGQDs because of Mn doping.

LGQDs and Mn-LGQDs is attributed to the stretching vibration of C-SO_x, confirming the presence of sulfur. It is worth noting that sulfur, in general, is known to be incorporated in the GQD lattice in the oxide form.[29,52] Based on previous studies, we expect that introduction of Mn dopant atoms into the graphitic lattice can occur either through substitutional doping or binding of Mn atoms onto N atoms.[24,53] In the first case, the Mn dopants are located ∼1.20 c5 above the vacancy of the graphene lattice.[53] Alternately, the Mn doping in nitrogen-containing GQDs can occur through the binding of Mn onto the doped lattice N atoms.[24] Here, a comparison of the FTIR spectrum between LGQDs and Mn-LGQDs demonstrated the disappearance of the N−H bending peak at 1484 cm^{-1}, pointing to the N-aided anchoring of Mn in Mn-LGQDs. Furthermore, the retention of higher N in Mn-LGQDs than LGQDs, based on the XPS analysis, also supports the N-assisted anchoring of Mn in Mn-LGQDs.

To assimilate a detailed understanding of individual elements in LGQDs, including their oxidation states, the high-resolution XPS scans of the elements (C, N, O, S, and Mn) were recorded, deconvoluted, and analyzed. The high-resolution scans of C 1s (Figures S8a and 2A1,B1) for lignosulfonate, LGQDs, and Mn-LGQDs were taken and deconvoluted, which signifies the existence of four types of carbons including graphitic carbon at 284.5 eV, C−O and C−N at 285.6 eV, C═O at 287.3 eV, and carbon bound to sulfur

https://dx.doi.org/10.1021/acssuschemeng.0c05789
ACS Sustainable Chem. Eng. 2020, 8, 16565−16576

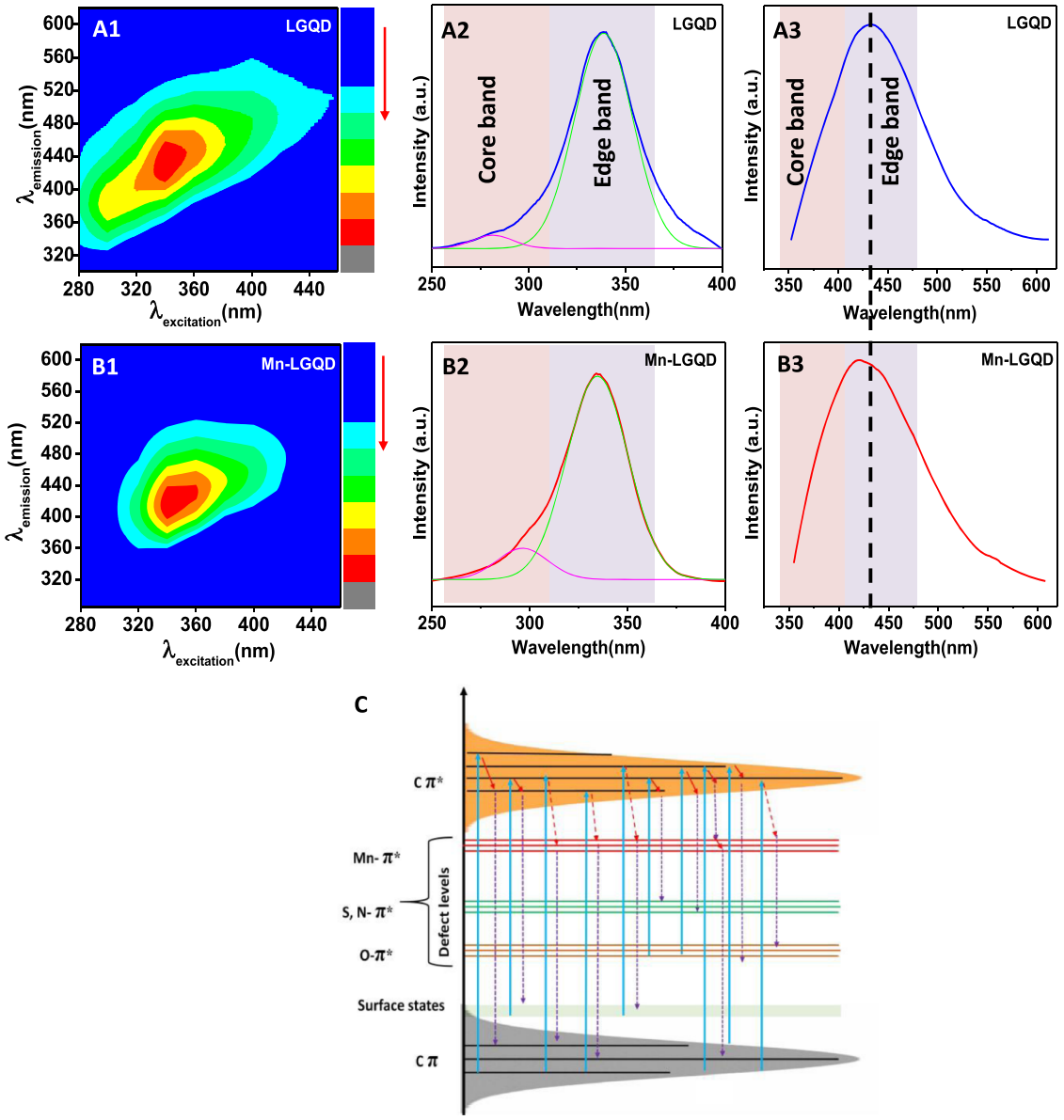

Figure 4. Photoluminescence (PL) studies of LGQDs and Mn-LGQDs with optimized doping. Excitation wavelength-dependent 2D PL excitation−emission contour maps of LGQDs (A1) and Mn-LGQDs (B1). The Z scale bars in the figures indicate the PL intensity. The PL excitation (PLE) spectra of LGQDs (A2) and Mn-LGQDs (B2).The PL emission spectrum of LGQDs (A3) and Mn-LGQDs (B3) under an excitation of 340 nm. (C) Schematic of the Mn-LGQD band structure, depicting different possible excitation and emission transitions.

(C-SO_x) at 286.53 eV. Notably, the C═C component is the most intense peak among all deconvoluted peaks in all GQD samples, implying the graphitic structure. Moreover, the increased carbon content in LGQDs compared to lignosulfonates is due to the cleavage of ether bonds and refusion into the aromatic skeletons. The deconvoluted high-resolution spectrum of N 1s indicated the existence of nitrogen in two different configurations, namely, graphitic (basal plane) and pyridinic (edge) N, represented by the components at binding energies 405 and 398 eV, respectively (Figure 2A2,B2). The pyridinic N peak at 398.5 eV may have covered the N−H peak observed at ∼401 eV.[54] It is worth noting that the pyridinic nitrogen content is more in Mn-LGQDs. The additional electron pairs provided by the pyridinic N atoms to the π cloud can result in the delocalization of electrons, thus potentially contributing to enhanced photophysical properties in Mn-LGQDs (discussed later).[55] We also analyzed that the high-resolution sulfur spectrum and the S 2p feature at ∼ 168.65 eV confirm sulfur doping in the oxide-S form in LGQDs as well as Mn-LGQDs (Figure 2A3,B3). The absence of $2p_{3/2}$ (∼164 eV) and $2p_{1/2}$ peaks (∼165 eV) in the S2p spectra excludes the possibility of sulfur existing in the thiophene form.[29] For Mn-LGQDs, we analyzed the Mn 2p region, which indicated that Mn exists in the Mn^{2+} state, bound to the N atoms in Mn-LGQDs (Figure S9). After understanding the structure and surface chemistry, we investigated the optical properties of LGQDs and Mn-LGQDs. The optical properties of GQDs are controlled by their size and electronic structure (e.g., band gap, surface functional groups, and defect density).[56] Because our morphological and topographical analyses (via TEM and AFM) indicated similar sizes for LGQDs and Mn-LGQDs, the doping-induced changes in the electronic structure should dictate their optical properties. We analyzed their absorption and emission spectra to unravel the doping effect on the

https://dx.doi.org/10.1021/acssuschemeng.0c05789
ACS Sustainable Chem. Eng. 2020, 8, 16565−16576

photophysical properties of LGQDs. The UV−vis absorption spectrum of lignosulfonate demonstrated a peak below 300 nm, characteristic of the aromatic units (Figure S10). Interestingly, the absorption spectrum of LGQDs (Figure 3a) showed two distinct absorption peaks around 270 and >300 nm. The first peak (~270 nm) is due to $\pi-\pi^*$ transition of C═C bond (generally referred to as the core band).[27] The second absorption peak at >300 nm is a result of both the $n-\pi^*$ transitions of C−N, C−S, and C═O/C−O groups and the $\pi-\pi^*$ charge−transfer transition of the GQD edge (edge band).[27,57] Similarly, the UV−vis absorption spectra of Mn-LGQDs also displayed two bands corresponding to the core (<300 nm) and edge-band (>300 nm) transitions (Figure 3b,c). However, the wavelengths corresponding to the maximum absorption ($\lambda_{abs,max}$) of the core and edge bands for Mn-LGQDs showed a slight shift compared to the corresponding peak maximum observed in the case of LGQDs. It is to be noted that $\pi-\pi^*$ (representing HOMO−LUMO) transition typically corresponds to the band gap, and therefore, the shift in $\pi-\pi^*$ transition maximum should be a consequence of band gap change that may occur because of changes in GQD size and/or doping.[27] Because the sizes of LGQDs and Mn-GQDs were found to be almost identical, we attribute the shift observed in the $\pi-\pi^*$band of Mn-LGQDs compared to LGQDs to the band structure modifications due to the introduction of Mn-dopant atoms.

To confirm the doping-induced band gap changes, we compared the optical band gap values of both LGQDs and Mn-LGQDs, which were calculated by employing the Tauc relation on UV−vis absorption data (Figure 3d,e). The Tauc relation[58] used for the optical band gap calculation is given by

$$(\alpha h\upsilon)^{1/n} = \alpha_0(h\upsilon - E_g) \quad (1)$$

where α, $h\upsilon$, α_0, E_g, and n are the absorption coefficient, photon energy, a constant, optical band gap, and an empirical constant, respectively. Here, α is obtained from the UV−vis absorption spectrum measurements. Typically, n values of 1/2 and 2 are assumed for calculating the band gaps of direct and indirect band gap semiconductors. Assuming LGQDs/Mn-LQGDs are direct band gap materials,[58] we used n = 1/2 in this study. Figure 3d,e shows the $(\alpha h\upsilon)^2$ versus hυ graphs for LGQDs and Mn-LGQDs. As shown in these graphs, the optical band gap (E_g) is given by the intercept of the linear fit of the $(\alpha h\upsilon)^2$ versus $h\upsilon$ curves with the energy ($h\upsilon$) axis. The optical band gaps estimated from these fits are 2.7 eV for LGQDs and 2.8 eV for Mn-LGQDs. From our results, it is clear that the introduction of Mn atoms resulted in a higher band gap for Mn-LGQDs compared to LGQDs, and therefore, we can confirm that the observed blue shift in the core-band peak is due to the higher band gap of Mn-LGQDs. The absorption peaks corresponding to edge transitions (Figure 3c) also showed a similar trend, with a ~47 nm blue shift in Mn-LGQDs compared to LGQDs. A schematic band diagram depicting the HOMO−LUMO level positions and band gaps for both LGQDs and Mn-LGQDs is presented in Figure 3f. The exact energy values of the HOMO and LUMO for the LGQDs and Mn-LGQDs were calculated from LSV scans, as shown in Figure S11. The corresponding calculations are explained in S20 (Supporting Information).

To comprehend the doping-dependent luminescence, we investigated the photoluminescence excitation (PLE) and emission spectra (PL) of the LGQDs and Mn-LGQDs as a function of excitation wavelengths (λ_{ex}) in the range of 280−460 nm. Figure 4A1,B1 shows the corresponding PL spectra contour maps with the Z scale bar, indicating the PL emission intensity of LGQDs and Mn-LGQDs at each point in the maps. From Figure 4A1,B1, it is clear that both spectral range and the peak wavelength of the PL spectra ($\lambda_{em,max}$) shift as a function of λ_{ex}. The excitation-dependent emissive properties of the LGQDs and Mn-LGQDs could be plausibly due to the distribution of multiple emissive centers on the quantum dots. Similar to the UV−vis absorption spectrum, the PLE spectrum of LGQDs and Mn-LGQDs also consists of two characteristic bands in the UV regime, with their peaks centered around ~290 and ~340 nm, which are ascribed to the core and edge bands. It is to be noted that the small differences (stokes shift) between the UV−vis absorption spectrum and PLE are commonly observed in chemically prepared GQDs.[27] The coexistence of two PLE bands in LGQDs and Mn-LGQDs further confirms the presence of multiple-emissive centers in LGQDs (Figure 4A2,B2). Another similarity observed in the PLE spectra of LGQDs and Mn-LGQDs is that the PLE peak at ~340 nm has a higher intensity than the PLE peak at ~290 nm. The relatively higher intensity of the edge bands implies that they are the dominant emissive centers in both LGQDs and Mn-LGQDs. Subsequently, we investigated the PL spectra of the LGQDs and Mn-LGQDs to validate the emissive centers and the changes induced by doping. The PL intensity maximum ($\lambda_{em,max}$) for LGQDs and Mn-LGQDs were observed at 440 and 420 nm (blue-shifted), respectively, when excited at 340 nm. Similar to the absorption spectrum, the PL spectra (Figure 4A3,B3) also showed two coexisting components (ascribed to the core and edge bands), again confirming the presence of two emissive centers in LGQDs and Mn-LGQDs. It is important to note that, in both PLE and PL spectra, the doping resulted in significant changes in band-II (edge-band transition) compared to band-I (core-band transition). This is understandable because doping is known to create edge states, which will play a significant role in PL. Consistent with the absorption spectra, a blue shift was observed for the edge band in Mn-LGQDs (Figure 4B3). Besides the edge bands, the PL core bands also showed a shift with doping. The core-band peaks (Figure 4A3,B3) in the case of Mn-LGQDs show a blue shift in comparison to the core-band peak of LGQDs. This shift can be attributed to the modification of electronic band structure (e.g., shifts in HOMO−LUMO levels) in Mn-LGQDs compared to LGQDs via the introduction of dopant atoms in the graphenic lattice, as observed in the band structure.[27,59] It is worth noting that PLE, in contrast to PL, did not show a considerable increase in intensity with doping (Figure 3a) because the PLE transitions correspond to transitions from the ground state ($C\pi$) to surface states. The doping-induced band structure changes can show a profound effect on the PLQY, an important metric used to represent the fluorescence efficiency of LGQDs and Mn-LGQDs quantitatively. The PLQY values for both these samples were estimated using the QY of quinine sulfate as a standard (S21, Supporting Information). The calculated QY for LGQDs is 23%, which is higher than those in most of the previously reported works on lignin-derived GQDs as well as some GQDs prepared from other precursors/methods (Table S1). The high PLQY in LGQDs can be ascribed to the in situ S and N doping effect due to the presence of sulfur and nitrogen in the lignosulfonate precursor. Similarly, the incorporation of Mn in Mn-LGQDs resulted in a

https://dx.doi.org/10.1021/acssuschemeng.0c05789
ACS Sustainable Chem. Eng. 2020, 8, 16565−16576

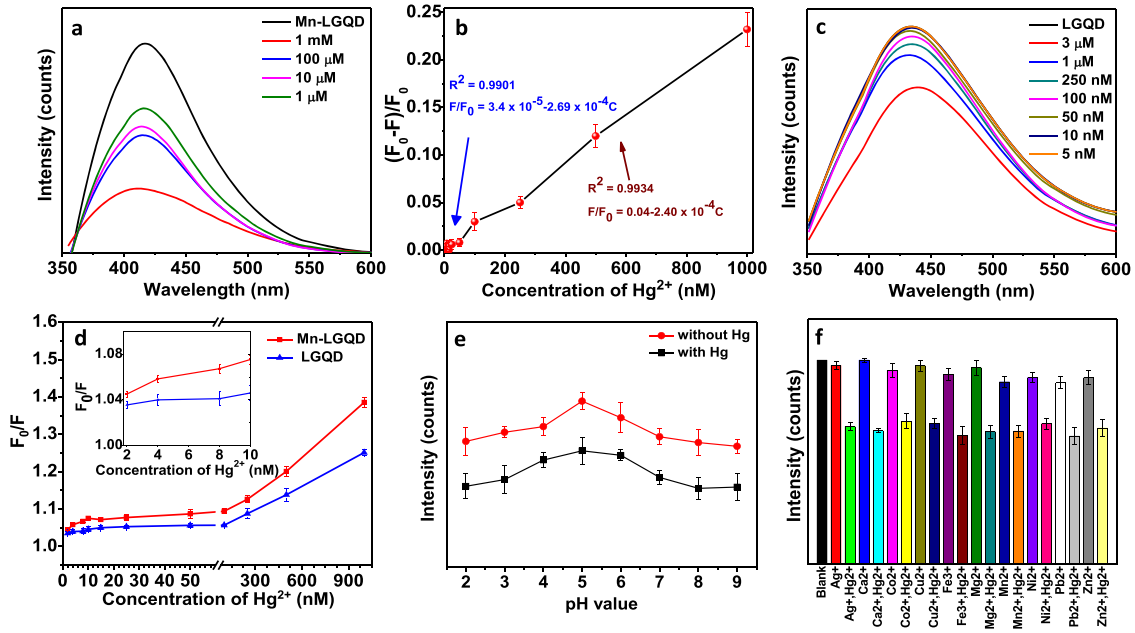

Figure 5. Fluorescence-based mercury detection studies using LGQDs and Mn-LGQDs. (a) PL spectra (λ_{ex} = 340 nm) of Mn-LGQDs measured in the presence of different concentrations of Hg^{2+}. (b) Plots of intensity ratio (F/F_0) versus the concentrations of Hg^{2+} in the case of Mn-LGQDs. (c) PL emission spectra (λ_{ex} = 340 nm) of LGQDs measured in the presence of different concentrations of Hg^{2+}. (d) Stern−Volmer plot for LGQD and Mn-LGQD. (e) Variation in PL maximum of Mn-LGQDs before and after the addition of 10 μM Hg^{2+} ions as a function of the pH value. (f) PL responses of Mn-LGQDs to the different metal ions with and without Hg^{2+}.

substantially higher PLQY (estimated as 31%, which is ∼35% enhancement in PLQY compared to LGQDs), indicating the effectiveness of metal−nonmetal codoping. The enhanced PLQY observed for Mn-LGQDs in comparison to LGQDs could be plausibly due to a synergistic effect of multiatom doping and a relatively higher number of "defect sites".[60] The defects can potentially create new energy levels between C π and π^*, thus providing new electron transition pathways in the band structure of Mn-LGQDs. The proposed energy-band diagram for the Mn-LGQD system (shown in Figure 4C) depicts the electronic absorption, interband crossing, and radiative emission through the energy levels, including HOMO−LUMO levels of carbon, surface states, antibonding orbitals, and so on. All the possible radiative emission transition pathways that could contribute to the observed high PLQY in Mn-LGQDs are depicted in Figure 4C. Because PLE corresponding to the core band is weak, the radiative PLE should predominately occur from the defect levels created because of Mn doping. Furthermore, we postulate that the peak PLE in Mn-LGQDs is blue-shifted, as new defect levels related to Mn doping are located closer to the C π^* level. Therefore, the electrons in the excited C π^* state can now transition to Mn π^* via interband crossing and then relax to the ground state via radiative emission. In addition, it has been reported that metal doping can result in charge transfer, accelerating the electron mobility on the GQD surface, and the presence of valence electrons in the dopant metal could be utilized to enhance the QY.[61,62] Figure S12 shows a schematic band diagram of LGQDs depicting the possible excitation and emission transitions. It is important to note that compared to Mn-LGQDs, there are fewer number of edge states in LGQDs, leading to a lower QY.

In addition to the changes in the material properties, including electronic band structure and surface chemistry of LGQDs/Mn-LGQDs, the solution's pH can also influence the PL properties. Therefore, we investigated the effect of pH on PL (Figure S13) for LGQDs and Mn-LGQDs. The results indicated that the emission intensity remains relatively stable at moderate pH, with a maximum PL observed at a pH of 5. However, a reduced PL intensity was observed under strongly acidic or alkaline conditions. The comparatively low PL at extreme pH conditions could be due to the protonation and deprotonation of functional groups at the edge of the Mn-LGQDs (and LGQDs) and the resultant aggregation.[41,63−65] In addition to the PLQY, a stable PL emission under continuous irradiation is another important requirement for practical applications.[66,67] The PL spectra measured under continuous irradiation showed a stable PL emission intensity, indicating that LGQDs/Mn-LGQDs are resistant to photobleaching (Figure S14).

The high PLQY coupled with stable luminescence at moderate pH ranges suggests that Mn-LGQDs are suitable for luminescence-based applications such as bioimaging and biosensing. Here, we investigated the utility of Mn-LGQDs and LGQDs with the maximum PLQY for sensing contaminants present in water bodies. Considering the acute toxicity of mercuric ions even at ultralow concentrations,[40] inorganic mercury was selected as the model contaminant. We studied the changes in the PL spectra of Mn-LGQDs and LGQDs after adding mercuric (Hg^{2+}) ions to the Mn-LGQD and LGQD solutions. The PL intensities of both LGQD and Mn-LGQD systems decreased with an increase in the Hg^{2+} concentration. Figure 5a shows the corresponding Hg^{2+} concentration-dependent PL emission spectra of Mn-LGQDs. As shown, with an increase in the Hg^{2+} ion concentration, the intensity of maximum emission peak (at 420 nm) in the PL spectra of Mn-LGQDs decreased without any change in the peak position. The concentration-dependent intensity changes confirm that the Mn-LGQDs with a high PLQY can be leveraged as a sensitive reporter for detecting

https://dx.doi.org/10.1021/acssuschemeng.0c05789
ACS Sustainable Chem. Eng. 2020, 8, 16565−16576

Hg^{2+} ions in the solution. The decrease in PL emission intensity followed a linear trend, as we increase the Hg^{2+} concentration in the Mn-LGQD solution in the range of 2−100 nM (inset of Figure 5b). By plotting the changes in the fluorescence intensity with concentration, the limit of detection (LOD) is estimated to be 0.56 nM. This estimated LOD of 0.56 nM is considerably lower compared to the LOD values of other fluorescent probes reported previously (Table S1). The existence of two linear regions with different slopes can be seen for higher (200 nM to 1 μM) and lower (1−100 nM) concentrations in Figure 5b.[68,69] The LOD is calculated here is for the lower concentration regime using the formula LOD = $3\sigma/s$, where σ is the standard deviation of the lowest signal and s is the slope of the linear fit.

Additionally, the mercury detection capability of LGQDs was also studied (Figure 5c) and compared with the performance of Mn-LGQDs. The LOD for Hg^{2+} detection using LGQDs is estimated to be 7 nM. The better (i.e., lower) LOD of Mn-LGQDs compared to LGQDs could be due to superior binding affinity of Hg^{2+} ions to the functional groups on the surface of the Mn-LGQDs.[24] It is worth noting that the augmented LOD of Mn-LGQDs (0.56 nM) for Hg^{2+} detection achieved through metal doping in this work is well below the allowed upper limit of Hg^{2+} ion levels in drinking water around the world.[70]

The observed PL quenching is potentially due to increased nonradiative decay of excited-state electrons via adjacent energy levels of the Hg^{2+} ions (Figure S15). The fluorescence quenching, because of nonradiative decay, in the presence of quenching molecules (or analytes) was modeled using the Stern−Volmer equation given as follows

$$F_0/F = 1 + K_{SV}C \quad (2)$$

where F and F_0 are the fluorescence intensities in the presence and absence of quenchers, respectively, K_{SV} is the Stern−Volmer quenching constant, and C is the concentration of the quencher or analyte.[30] The fluorescence kinetics can be analyzed using K_{SV}, which is a product of reaction rate constant (k_q) and the lifetime of emissive excited states (τ_0) without the presence of quenching molecules. The K_{SV} values given by the slope of the Stern−Volmer equation are 3.49×10^5 M^{-1} and 2.19×10^5 M^{-1} for Mn-LGQDs and LGQDs, respectively (Figure 5d). The high K_{SV} value (which is also a measure of the sensitivity of the luminescence-based sensors) of Mn-LGQDs compared to LGQDs can be attributed to increase in their reaction rate constant, again pointing to the increased affinity of Hg^{2+} toward Mn-LGQDs. However, detailed investigations including time-dependent PL studies are required to confirm the quenching mechanism.

Furthermore, we investigated the effect of the solution pH on the Hg^{2+} detection capabilities of Mn-LGQDs. For this, the PL spectra of Mn-LGQDs were recorded by introducing Hg^{2+} under different pH conditions. These PL results suggest that the quenching efficiency is constant in both high acidic and alkaline conditions (Figure 5e), implying that Mn-LGQDs can detect Hg^{2+} across all pH ranges. For practical applications, it is critical to ensure that the fluorescent Mn-LGQD probes are also selective toward Hg^{2+} ions (i.e., analytes of interest). To test the selectivity of Mn-LGQDs, we studied the PL spectra of Mn-LGQD solutions by mixing them with different metal ion solutions (5 μM) including Cu^{2+}, Mn^{2+}, Ag^{+}, Pb^{2+}, K^{+}, Zn^{2+}, Ca^{2+}, Co^{2+}, Hg^{2+}, Fe^{3+}, Ni^{2+}, and Mg^{2+}. From these results, it can be inferred that the PL intensity of Mn-LGQDs is quenched by Hg^{2+} ions only, while all other metal ions showed no significant interference (Figure 5f), thus confirming the high selectivity of Mn-LGQDs toward Hg^{2+} over other metal ions. Additionally, to test the influence of mercury salt (anion effect), we conducted PL quenching studies using two different mercury salts. The Mn-LGQDs exhibited a similar PL quenching response to both Hg^{2+} sources tested (chloride and nitrate salts), implying that the quenching phenomenon is indeed a direct consequence of Hg^{2+} ions (Figure S16) and is not influenced by the anion species. To confirm the reusability of our samples, the ability of Mn-GQDs to restore PL (after being quenched by mercuric ions) was investigated. For this, EDTA, a chelating agent with high affinity toward Hg^{2+} ions, was introduced into the Mn-GQD-Hg (II) system. When EDTA is added to the solution that contains mercury salt and GQDs, owing to the higher complexation constant between EDTA and Hg,[71−73] Hg^{2+} ions detach from the GQDs and chelate the Hg^{2+} ions to form the EDTA−Hg complex. The removal of Hg^{2+} from the GQDs leads to the disaggregation of Mn-LGQDs and finally restores PL. The partial restoration of PL from the PL-quenched sample at Hg^{2+} concentrations of 250 and 1000 nM is shown in Figure S17. Furthermore, to check their reusability, we used the Mn-GQD sample, whose PL was restored for detecting Hg^{2+} (Figure S18). A similar change in the PL intensity upon addition illustrated their reusability. We also conducted the capability of Mn-GQDs to detect Hg^{2+} in real water samples as well. Figure S19 shows the detection of Hg^{2+} at various concentrations conducted using tap water, which confirms the practical utility of the Mn-LGQD samples. We have also evaluated some of the relevant sustainability parameters to understand the "greenness" of the material as well as the synthesis method (S22, Supporting Information).[74,75] Therefore, the lignosulfonate precursor-derived Mn-LGQDs offer a highly sustainable, sensitive, and selective fluorescent platform for detecting Hg^{2+} in water samples.

CONCLUSIONS

In summary, we synthesized metal- and nonmetal-codoped GQDs from lignosulfonate (Mn-LGQDs) via an efficient and sustainable synthetic strategy. An in-depth microscopic and spectroscopic characterization study confirmed the in situ S and N doping in lignosulfonate-derived LGQDs as a consequence of S and N atoms present in the precursor. The in situ doping also helps to easily integrate metal and nonmetal in the GQD matrix. The LGQDs and Mn-LGQDs exhibited excellent PL and photostabilities. The metal and nonmetal codoping in Mn-LGQDs results in significantly enhanced PLQY, making them a viable candidate for a variety of fluorescence-based sensing applications. The wavelength-dependent PL measurements of LGQDs and Mn-LGQDs indicate the existence of multiple emissive centers, with core band, resulting from carbon $\pi-\pi^*$ transitions in the sp^2 domain, and the edge band, originating from both the $n-\pi^*$ and $\pi-\pi^*$ transitions. Furthermore, we successfully demonstrated that Mn-LGQDs prepared using lignosulfonate have a very low LOD in addition to excellent selectivity and high sensitivity for detecting Hg^{2+} in polluted water. This study demonstrates the potential of lignosulfonate-derived GQDs as an alternative, environmentally friendly, and cost-effective fluorescent probes for detecting toxic metal ions in water.

https://dx.doi.org/10.1021/acssuschemeng.0c05789
ACS Sustainable Chem. Eng. 2020, 8, 16565−16576

■ ASSOCIATED CONTENT

Supporting Information

The Supporting Information is available free of charge at https://pubs.acs.org/doi/10.1021/acssuschemeng.0c05789.

Influence of process parameters on PL, influence of Mn dopant percentage on PL, XPS survey spectrum of lignosulfonate, XRD of LGQDs, TEM and HRTEM of Mn-LGQDs, AFM images of Mn-LGQDs and LGQDs, FTIR spectrum of lignosulfonate, LGQD, and Mn-LGQD, high-resolution XPS spectrum of lignosulfonate, high-resolution XPS spectrum of Mn in Mn-LGQDs, UV−vis measurement of lignosulfonate, linear sweep voltammetry measurements, band structure of LGQDs with possible excitations and emission transitions, influence of pH on PL of LGQDs and Mn-LGQDs, photostability measurements of LGQDs and Mn-LGQDs, quenching of fluorescence of Mn-LGQDs in the presence of Hg^{2+} ions, anion effect on PL quenching of Mn-LGQDs, PL regain of Mn-LGQDs using EDTA, durability study of Mn-LGQDs, mercury sensing conducted using tap water, calculation of HOMO and LUMO levels, quantum yield measurements, sustainability metrics calculation, and performance of different quantum dots synthesized using different techniques (PDF)

■ AUTHOR INFORMATION

Corresponding Author

Sreeprasad T. Sreenivasan − *Department of Chemistry and Biochemistry, The University of Texas at El Paso, El Paso, Texas 79968, United States;* orcid.org/0000-0002-5728-0512; Phone: 915-747-6833; Email: sreenivasan@utep.edu; Fax: 915-747-5748

Authors

Aruna N. Nair − *Department of Chemistry and Biochemistry, The University of Texas at El Paso, El Paso, Texas 79968, United States*

Venkata S.N. Chava − *Department of Chemistry and Biochemistry, The University of Texas at El Paso, El Paso, Texas 79968, United States*

Saptasree Bose − *Department of Chemistry and Biochemistry, The University of Texas at El Paso, El Paso, Texas 79968, United States*

Ting Zheng − *Department of Automotive Engineering and Clemson Composites Centre, Clemson University, Greenville, South Carolina 29607, United States;* orcid.org/0000-0002-4115-4626

Srikanth Pilla − *Department of Automotive Engineering, Clemson Composites Centre, Department of Materials Science and Engineering, and Department of Mechanical Engineering, Clemson University, Greenville, South Carolina 29607, United States;* orcid.org/0000-0003-3728-6578

Complete contact information is available at: https://pubs.acs.org/10.1021/acssuschemeng.0c05789

Funding

The work was supported through the UTEP start-up grant, UT STARs award, UTEP-URI award, and NSF-PREM grant #DMR-1827745.

Notes

The authors declare no competing financial interest.

■ ACKNOWLEDGMENTS

We gratefully acknowledge Dr. Mahesh Narayan for providing us access to the fluorescence spectrometer and thought-provoking discussions.

■ REFERENCES

(1) Zhang, Z.; Zhang, J.; Chen, N.; Qu, L. Graphene quantum dots: an emerging material for energy-related applications and beyond. *Energy Environ. Sci.* **2012**, *5*, 8869−8890.

(2) Kumawat, M. K.; Thakur, M.; Gurung, R. B.; Srivastava, R. Graphene quantum dots from mangifera indica: application in near-infrared bioimaging and intracellular nanothermometry. *ACS Sustainable Chem. Eng.* **2017**, *5*, 1382−1391.

(3) Son, D. I.; Kwon, B. W.; Park, D. H.; Seo, W.-S.; Yi, Y.; Angadi, B.; Lee, C.-L.; Choi, W. K. Emissive ZnO−graphene quantum dots for white-light-emitting diodes. *Nat. Nanotechnol.* **2012**, *7*, 465−471.

(4) Sreeprasad, T. S.; Nguyen, P.; Alshogeathri, A.; Hibbeler, L.; Martinez, F.; McNeil, N.; Berry, V. Graphene quantum dots interfaced with single bacterial spore for bio-electromechanical devices: a graphene cytobot. *Sci. Rep.* **2015**, *5*, 9138.

(5) Liu, Y.; Wei, J.; Yan, X.; Zhao, M.; Guo, C.; Xu, Q. Barium charge transferred doped carbon dots with ultra-high quantum yield photoluminescence of 99.6% and applications. *Chin. Chem. Lett.* **2020**, DOI: 10.1016/j.cclet.2020.05.037.

(6) Xu, Q.; Liu, Y.; Su, R.; Cai, L.; Li, B.; Zhang, Y.; Zhang, L.; Wang, Y.; Wang, Y.; Li, N.; Gong, X.; Gu, Z.; Chen, Y.; Tan, Y.; Dong, C.; Sreeprasad, T. S. Highly fluorescent Zn-doped carbon dots as Fenton reaction-based bio-sensors: an integrative experimental−theoretical consideration. *Nanoscale* **2016**, *8*, 17919−17927.

(7) Fan, L.; Zhu, M.; Lee, X.; Zhang, R.; Wang, K.; Wei, J.; Zhong, M.; Wu, D.; Zhu, H. Direct synthesis of graphene quantum dots by chemical vapor deposition. *Part. Part. Syst. Char.* **2013**, *30*, 764−769.

(8) Liu, R.; Wu, D.; Feng, X.; Müllen, K. Bottom-up fabrication of photoluminescent graphene quantum dots with uniform morphology. *J. Am. Chem. Soc.* **2011**, *133*, 15221−15223.

(9) Tang, L.; Ji, R.; Cao, X.; Lin, J.; Jiang, H.; Li, X.; Teng, K. S.; Luk, C. M.; Zeng, S.; Hao, J.; Lau, S. P. Deep ultraviolet photoluminescence of water-soluble self-passivated graphene quantum dots. *ACS Nano* **2012**, *6*, 5102−5110.

(10) Atienzar, P.; Primo, A.; Lavorato, C.; Molinari, R.; García, H. Preparation of graphene quantum dots from pyrolyzed alginate. *Langmuir* **2013**, *29*, 6141−6146.

(11) Prasannan, A.; Imae, T. One-pot synthesis of fluorescent carbon dots from orange waste peels. *Ind. Eng. Chem. Res.* **2013**, *52*, 15673−15678.

(12) Tan, X. W.; Romainor, A. N. B.; Chin, S. F.; Ng, S. M. Carbon dots production via pyrolysis of sago waste as potential probe for metal ions sensing. *J. Anal. Appl. Pyrol.* **2014**, *105*, 157−165.

(13) Chen, W.; Li, D.; Tian, L.; Xiang, W.; Wang, T.; Hu, W.; Hu, Y.; Chen, S.; Chen, J.; Dai, Z. Synthesis of graphene quantum dots from natural polymer starch for cell imaging. *Green Chem.* **2018**, *20*, 4438−4442.

(14) Wang, Z.; Yu, J.; Zhang, X.; Li, N.; Liu, B.; Li, Y.; Wang, Y.; Wang, W.; Li, Y.; Zhang, L.; Dissanayake, S.; Suib, S. L.; Sun, L. Large-scale and controllable synthesis of graphene quantum dots from rice husk biomass: a comprehensive utilization strategy. *ACS Appl. Mater. Interfaces* **2016**, *8*, 1434−1439.

(15) Ding, Z.; Li, F.; Wen, J.; Wang, X.; Sun, R. Gram-scale synthesis of single-crystalline graphene quantum dots derived from lignin biomass. *Green Chem.v* **2018**, *20*, 1383−1390.

(16) Park, S. Y.; Lee, H. U.; Park, E. S.; Lee, S. C.; Lee, J.-W.; Jeong, S. W.; Kim, C. H.; Lee, Y.-C.; Huh, Y. S.; Lee, J. Photoluminescent green carbon nanodots from food-waste-derived sources: large-scale synthesis, properties, and biomedical applications. *ACS Appl. Mater. Interfaces* **2014**, *6*, 3365−3370.

(17) Suryawanshi, A.; Biswal, M.; Mhamane, D.; Gokhale, R.; Patil, S.; Guin, D.; Ogale, S. Large scale synthesis of graphene quantum dots (GQDs) from waste biomass and their use as an efficient and selective

photoluminescence on−off−on probe for Ag+ ions. *Nanoscale* **2014**, *6*, 11664−11670.
(18) Bajwa, D. S.; Pourhashem, G.; Ullah, A. H.; Bajwa, S. G. A concise review of current lignin production, applications, products and their environmental impact. *Ind. Crops Prod.* **2019**, *139*, 111526.
(19) Fache, M.; Boutevin, B.; Caillol, S. Vanillin production from lignin and its use as a renewable chemical. *ACS Sustain. Chem. Eng.* **2015**, *4*, 35−46.
(20) Chatterjee, S.; Jones, E. B.; Clingenpeel, A. C.; McKenna, A. M.; Rios, O.; McNutt, N. W.; Keffer, D. J.; Johs, A. Conversion of lignin precursors to carbon fibers with nanoscale graphitic domains. *ACS Sustainable Chem. Eng.* **2014**, *2*, 2002−2010.
(21) Chatterjee, S.; Saito, T. Lignin-derived advanced carbon materials. *ChemSusChem* **2015**, *8*, 3941−3958.
(22) Wang, H.; Ben, H.; Ruan, H.; Zhang, L.; Pu, Y.; Feng, M.; Ragauskas, A. J.; Yang, B. Effects of lignin structure on hydrodeoxygenation reactivity of pine wood lignin to valuable chemicals. *ACS Sustainable Chem. Eng.* **2017**, *5*, 1824−1830.
(23) Behling, R.; Valange, S.; Chatel, G. Heterogeneous catalytic oxidation for lignin valorization into valuable chemicals: what results? What limitations? What trends? *Green Chem.* **2016**, *18*, 1839−1854.
(24) Yang, L.; Qin, A.; Chen, S.; Liao, L.; Qin, J.; Zhang, K. Manganese (II) enhanced fluorescent nitrogen-doped graphene quantum dots: a facile and efficient synthesis and their applications for bioimaging and detection of Hg 2+ ions. *RSC Adv.* **2018**, *8*, 5902−5911.
(25) Hao, Y.-N.; Guo, H.-L.; Tian, L.; Kang, X. Enhanced photoluminescence of pyrrolic-nitrogen enriched graphene quantum dots. *RSC Adv.* **2015**, *5*, 43750−43755.
(26) Gu, J.; Zhang, X.; Pang, A.; Yang, J. Facile synthesis and photoluminescence characteristics of blue-emitting nitrogen-doped graphene quantum dots. *Nanotechnology* **2016**, *27*, 165704.
(27) Yang, G.; Wu, C.; Luo, X.; Liu, X.; Gao, Y.; Wu, P.; Cai, C.; Saavedra, S. S. Exploring the emissive states of heteroatom-doped graphene quantum dots. *J. Phys. Chem. C* **2018**, *122*, 6483−6492.
(28) Wang, R.; Xia, G.; Zhong, W.; Chen, L.; Chen, L.; Wang, Y.; Min, Y.; Li, K. Direct transformation of lignin into fluorescence-switchable graphene quantum dots and their application in ultrasensitive profiling of a physiological oxidant. *Green Chem.* **2019**, *21*, 3343−3352.
(29) Li, X.; Lau, S. P.; Tang, L.; Ji, R.; Yang, P. Sulphur doping: a facile approach to tune the electronic structure and optical properties of graphene quantum dots. *Nanoscale* **2014**, *6*, 5323−5328.
(30) Gu, S.; Hsieh, C.-T.; Tsai, Y.-Y.; Ashraf Gandomi, Y.; Yeom, S.; Kihm, K. D.; Fu, C.-C.; Juang, R.-S. Sulfur and Nitrogen Co-Doped Graphene Quantum Dots as a Fluorescent Quenching Probe for Highly Sensitive Detection toward Mercury Ions. *ACS Appl. Nano Mater.* **2019**, *2*, 790−798.
(31) Kharangarh, P. R.; Gupta, V.; Singh, A.; Bhardwaj, P.; Grace, A. N. An efficient pseudocapacitor electrode material with co-doping of iron (II) and sulfur in luminescent graphene quantum dots. *Diamond Relat.Mater.* **2020**, *107*, 107913.
(32) Lin, L.; Song, X.; Chen, Y.; Rong, M.; Wang, Y.; Zhao, L.; Zhao, T.; Chen, X. Europium-decorated graphene quantum dots as a fluorescent probe for label-free, rapid and sensitive detection of Cu2+ and L-cysteine. *Anal.Chim. Acta* **2015**, *891*, 261−268.
(33) Lin, L.; Luo, Y.; Tsai, P.; Wang, J.; Chen, X. Metal ions doped carbon quantum dots: Synthesis, physicochemical properties, and their applications. *Trac. Trends Anal. Chem.* **2018**, *103*, 87−101.
(34) Pang, J.; Zhang, W.; Zhang, H.; Zhang, J.; Zhang, H.; Cao, G.; Han, M.; Yang, Y. Sustainable nitrogen-containing hierarchical porous carbon spheres derived from sodium lignosulfonate for high-performance supercapacitors. *Carbon* **2018**, *132*, 280−293.
(35) Xu, Q.; Liu, Y.; Gao, C.; Wei, J.; Zhou, H.; Chen, Y.; Dong, C.; Sreeprasad, T. S.; Li, N.; Xia, Z. Synthesis, mechanistic investigation, and application of photoluminescent sulfur and nitrogen co-doped carbon dots. *J. Mater. Chem. C* **2015**, *3*, 9885−9893.
(36) Bian, S.; Shen, C.; Hua, H.; Zhou, L.; Zhu, H.; Xi, F.; Liu, J.; Dong, X. One-pot synthesis of sulfur-doped graphene quantum dots as a novel fluorescent probe for highly selective and sensitive detection of lead (II). *RSC Adv.* **2016**, *6*, 69977−69983.
(37) Liu, Z.; Mo, Z.; Niu, X.; Yang, X.; Jiang, Y.; Zhao, P.; Liu, N.; Guo, R. Highly sensitive fluorescence sensor for mercury (II) based on boron-and nitrogen-co-doped graphene quantum dots. *J. Colloid Interface Sci.* **2020**, *566*, 357−368.
(38) Guo, X.; Huang, J.; Wei, Y.; Zeng, Q.; Wang, L. Fast and selective detection of mercury ions in environmental water by paper-based fluorescent sensor using boronic acid functionalized MoS2 quantum dots. *J. Hazard. Mater.* **2020**, *381*, 120969.
(39) Mao, Y.; Zhao, C.; Ge, S.; Luo, T.; Chen, J.; Liu, J.; Xi, F.; Liu, J. Gram-scale synthesis of nitrogen doped graphene quantum dots for sensitive detection of mercury ions and L-cysteine. *RSC Adv.* **2019**, *9*, 32977−32983.
(40) Ye, B.-J.; Kim, B.-G.; Jeon, M.-J.; Kim, S.-Y.; Kim, H.-C.; Jang, T.-W.; Chae, H.-J.; Choi, W.-J.; Ha, M.-N.; Hong, Y.-S. Evaluation of mercury exposure level, clinical diagnosis and treatment for mercury intoxication. *Ann. Occup. Environ. Med.* **2016**, *28*, 1−8.
(41) Wang, L.; Wang, Y.; Xu, T.; Liao, H.; Yao, C.; Liu, Y.; Li, Z.; Chen, Z.; Pan, D.; Sun, L.; Wu, M. Gram-scale synthesis of single-crystalline graphene quantum dots with superior optical properties. *Nat. Commun.* **2014**, *5*, 5357.
(42) Kadian, S.; Manik, G.; Kalkal, A.; Singh, M.; Chauhan, R. P. Effect of sulfur doping on fluorescence and quantum yield of graphene quantum dots: an experimental and theoretical investigation. *Nanotechnology* **2019**, *30*, 435704.
(43) Lingam, K.; Podila, R.; Qian, H.; Serkiz, S.; Rao, A. M. Evidence for Edge-State Photoluminescence in Graphene Quantum Dots. *Adv. Funct. Mater.* **2013**, *23*, 5062−5065.
(44) Li, L.; Dong, T. Photoluminescence tuning in carbon dots: Surface passivation or/and functionalization, heteroatom doping. *J. Mater. Chem. C* **2018**, *6*, 7944−7970.
(45) Shen, J.; Zhu, Y.; Yang, X.; Zong, J.; Zhang, J.; Li, C. One-pot hydrothermal synthesis of graphene quantum dots surface-passivated by polyethylene glycol and their photoelectric conversion under near-infrared light. *New J. Chem.* **2012**, *36*, 97−101.
(46) Li, X.; Zhang, S.; Kulinich, S. A.; Liu, Y.; Zeng, H. Engineering surface states of carbon dots to achieve controllable luminescence for solid-luminescent composites and sensitive Be 2+ detection. *Sci. Rep.* **2014**, *4*, 4976.
(47) Zhu, S.; Song, Y.; Zhao, X.; Shao, J.; Zhang, J.; Yang, B. The photoluminescence mechanism in carbon dots (graphene quantum dots, carbon nanodots, and polymer dots): current state and future perspective. *Nano Res.* **2015**, *8*, 355−381.
(48) Xu, Q.; Pu, P.; Zhao, J.; Dong, C.; Gao, C.; Chen, Y.; Chen, J.; Liu, Y.; Zhou, H. Preparation of highly photoluminescent sulfur-doped carbon dots for Fe (III) detection. *J. Mater. Chem. A* **2015**, *3*, 542−546.
(49) Ferrari, A. C.; Meyer, J. C.; Scardaci, V.; Casiraghi, C.; Lazzeri, M.; Mauri, F.; Piscanec, S.; Jiang, D.; Novoselov, K. S.; Roth, S.; Geim, A. K. Raman spectrum of graphene and graphene layers. *Phys. Rev. Lett.* **2006**, *97*, 187401.
(50) Zheng, X. T.; Than, A.; Ananthanaraya, A.; Kim, D.-H.; Chen, P. Graphene quantum dots as universal fluorophores and their use in revealing regulated trafficking of insulin receptors in adipocytes. *ACS Nano* **2013**, *7*, 6278−6286.
(51) Gliniak, J.; Lin, J.-H.; Chen, Y.-T.; Li, C.-R.; Jokar, E.; Chang, C.-H.; Peng, C.-S.; Lin, J.-N.; Lien, W.-H.; Tsai, H.-M.; Wu, T.-K. Sulfur-doped graphene oxide quantum dots as photocatalysts for hydrogen generation in the aqueous phase. *ChemSusChem* **2017**, *10*, 3260−3267.
(52) Xu, Y.; Li, D.; Liu, M.; Niu, F.; Liu, J.; Wang, E. Enhanced-quantum yield sulfur/nitrogen co-doped fluorescent carbon nanodots produced from biomass Enteromorpha prolifera: synthesis, posttreatment, applications and mechanism study. *Sci. Rep.* **2017**, *7*, 4499.
(53) Wu, M.; Cao, C.; Jiang, J. Z. Electronic structure of substitutionally Mn-doped graphene. *New J. Phys.* **2010**, *12*, 063020.

https://dx.doi.org/10.1021/acssuschemeng.0c05789
ACS Sustainable Chem. Eng. 2020, 8, 16565−16576

(54) Wang, R.; Xie, T.; Sun, Z.; Pu, T.; Li, W.; Ao, J.-P. Graphene quantum dot modified gC 3 N 4 for enhanced photocatalytic oxidation of ammonia performance. *RSC Adv.* **2017**, *7*, 51687−51694.
(55) Permatasari, F. A.; Aimon, A. H.; Iskandar, F.; Ogi, T.; Okuyama, K. Role of C−N configurations in the photoluminescence of graphene quantum dots synthesized by a hydrothermal route. *Sci. Rep.* **2016**, *6*, 21042.
(56) Jin, S. H.; Kim, D. H.; Jun, G. H.; Hong, S. H.; Jeon, S. Tuning the photoluminescence of graphene quantum dots through the charge transfer effect of functional groups. *ACS Nano* **2013**, *7*, 1239−1245.
(57) Sudolská, M.; Dubecký, M.; Sarkar, S.; Reckmeier, C. J.; Zbořil, R.; Rogach, A. L.; Otyepka, M. Nature of absorption bands in oxygen-functionalized graphitic carbon dots. *J. Phys. Chem. C* **2015**, *119*, 13369−13373.
(58) Yeh, T.-F.; Teng, C.-Y.; Chen, S.-J.; Teng, H. Nitrogen-doped graphene oxide quantum dots as photocatalysts for overall water-splitting under visible light Illumination. *Adv. Mater.* **2014**, *26*, 3297−3303.
(59) Wang, X.; Sun, G.; Routh, P.; Kim, D.-H.; Huang, W.; Chen, P. Heteroatom-doped graphene materials: syntheses, properties and applications. *Chem. Soc. Rev.* **2014**, *43*, 7067−7098.
(60) Qian, F.; Li, X.; Tang, L.; Lai, S. K.; Lu, C.; Lau, S. P. Potassium doping: tuning the optical properties of graphene quantum dots. *AIP Advances* **2016**, *6*, 075116.
(61) Xu, Q.; Su, R.; Chen, Y.; Theruvakkattil Sreenivasan, S.; Li, N.; Zheng, X.; Zhu, J.; Pan, H.; Li, W.; Xu, C.; Xia, Z.; Dai, L. Metal Charge Transfer Doped Carbon Dots with Reversibly Switchable, Ultra-High Quantum Yield Photoluminescence. *ACS Appl. Nano Mater.* **2018**, *1*, 1886−1893.
(62) Hui, W.; Yang, Y.; Xu, Q.; Gu, H.; Feng, S.; Su, Z.; Zhang, M.; Wang, J.; Li, X.; Fang, J.; Xia, F.; Xia, Y.; Chen, Y.; Gao, X.; Huang, W. Red-Carbon-Quantum-Dot-Doped SnO2 Composite with Enhanced Electron Mobility for Efficient and Stable Perovskite Solar Cells. *Adv. Mater.* **2020**, *32*, 1906374.
(63) Zhang, B.; Liu, Y.; Ren, M.; Li, W.; Zhang, X.; Vajtai, R.; Ajayan, P. M.; Tour, J. M.; Wang, L. Sustainable Synthesis of Bright Green Fluorescent Nitrogen-Doped Carbon Quantum Dots from Alkali Lignin. *ChemSusChem* **2019**, *12*, 4202−4210.
(64) Liu, G.; Li, S.; Cheng, M.; Zhao, L.; Zhang, B.; Gao, Y.; Xu, Y.; Liu, F.; Lu, G. Facile synthesis of nitrogen and sulfur co-doped carbon dots for multiple sensing capacities: alkaline fluorescence enhancement effect, temperature sensing, and selective detection of Fe 3+ ions. *New J. Chem.* **2018**, *42*, 13147−13156.
(65) Park, C. H.; Yang, H.; Lee, J.; Cho, H.-H.; Kim, D.; Lee, D. C.; Kim, B. J. Multicolor emitting block copolymer-integrated graphene quantum dots for colorimetric, simultaneous sensing of temperature, pH, and metal ions. *Chem. Mater.* **2015**, *27*, 5288−5294.
(66) Wang, L.; Li, W.; Li, M.; Su, Q.; Li, Z.; Pan, D.; Wu, M. Ultrastable amine, sulfo cofunctionalized graphene quantum dots with high two-photon fluorescence for cellular imaging. *ACS Sustainable Chem. Eng.* **2018**, *6*, 4711−4716.
(67) Ma, M.; Hu, X.; Zhang, C.; Deng, C.; Wang, X. The optimum parameters to synthesize bright and stable graphene quantum dots by hydrothermal method. *J. Mater. Sci.: Mater. Electron.* **2017**, *28*, 6493−6497.
(68) Ma, Y.; Chen, A. Y.; Xie, X. F.; Wang, X. Y.; Wang, D.; Wang, P.; Li, H. J.; Yang, J. H.; Li, Y. Doping effect and fluorescence quenching mechanism of N-doped graphene quantum dots in the detection of dopamine. *Talanta* **2019**, *196*, 563−571.
(69) Liu, Y.; Tang, X.; Deng, M.; Cao, Y.; Li, Y.; Zheng, H.; Li, F.; Yan, F.; Lan, T.; Shi, L.; Gao, L.; Huang, L.; Zhu, T.; Lin, H.; Bai, Y.; Qu, D.; Huang, X.; Qiu, F. Nitrogen doped graphene quantum dots as a fluorescent probe for mercury (II) ions. *Microchim. Acta* **2019**, *186*, 140.
(70) Cotruvo, J. A. 2017 WHO Guidelines for Drinking Water Quality: First Addendum to the Fourth Edition. *J. Am. Water Works Assoc.* **2017**, *109*, 44−51.
(71) Wu, Z.; Feng, M.; Chen, X.; Tang, X. N-dots as a photoluminescent probe for the rapid and selective detection of Hg 2+ and Ag+ in aqueous solution. *J. Mater. Chem. B* **2016**, *4*, 2086−2089.
(72) Chakraborti, H.; Sinha, S.; Ghosh, S.; Pal, S. K. Interfacing water soluble nanomaterials with fluorescence chemosensing: Graphene quantum dot to detect Hg2+ in 100% aqueous solution. *Mater.Lett.* **2013**, *97*, 78−80.
(73) Kappen, J.; Ponkarpagam, S.; John, S. A. Study on the interactions between graphene quantum dots and Hg (II): Unraveling the origin of photoluminescence quenching of graphene quantum dots by Hg (II). *Colloid.Surface.Physicochem.Eng. Aspect.* **2020**, *591*, 124551.
(74) Mukherjee, S.; Kumar, A. A.; Sudhakar, C.; Kumar, R.; Ahuja, T.; Mondal, B.; Srikrishnarka, P.; Philip, L.; Pradeep, T. Sustainable and affordable composites built using microstructures performing better than nanostructures for arsenic removal. *ACS Sustainable Chem. Eng.* **2018**, *7*, 3222−3233.
(75) Sheldon, R. A. Metrics of green chemistry and sustainability: past, present, and future. *ACS Sustainable Chem. Eng.* **2018**, *6*, 32−48.

https://dx.doi.org/10.1021/acssuschemeng.0c05789
ACS Sustainable Chem. Eng. 2020, 8, 16565−16576